High-performance self-powered ultraviolet photodetector based on PVK/amorphous-WO₃ organic-inorganic heterojunction

Menghan Jia[a,c], Libin Tang[b,c],*, Kar Seng Teng[d],*, and Yanfei Lü[a],*

[a] *School of Physics and Astronomy, Yunnan University, Kunming 650500, People's Republic of China*

[b] *Kunming Institute of Physics, Kunming 650223, People's Republic of China*

[c] *Yunnan State Key Laboratory of Advanced Photoelectric Materials and Devices, Kunming 650223, People's Republic of China*

[d] *Department of Electronic and Electrical Engineering, Swansea University, Bay Campus, Fabian Way, Swansea SA1 8EN, United Kingdom*

E-mail: scitang@163.com, k.s.teng@swansea.ac.uk, optik@sina.com

Abstract: Ultraviolet (UV) photodetectors have found wide-ranging applications, ranging from optical communications to chemical detection. High performance UV photodetectors that can be self-powered are highly desirable in many applications as they can minimize energy consumption during operation. Herein, a self-powered UV photodetector, which consisted of poly(9-vinylcarbazole) (PVK)/amorphous-WO₃ organic-inorganic heterojunction with PEDOT:PSS as a hole transport layer, was fabricated using a two-step method at low temperature. The effect of WO₃, PVK and PEDOT:PSS films on the performances of the photodetector was also investigated. Under optimized parameters, the PEDOT:PSS/PVK/WO₃ photodetector exhibited a maximum responsivity of 12.41 AW^{-1}, specific detectivity of 1.80×10^{13} Jones, photo-dark current ratio of 10^3 at reverse bias and typical rectification characteristic when exposed to 365 nm light irradiation. The photoelectric conversion mechanism of this novel PVK/WO₃ heterojunction is discussed using energy band diagrams. This work presents a method to produce a high performance WO₃-based heterostructure at low temperature, which has the potential for UV imaging.

Keywords: Self-powered; UV photodetector; Organic-inorganic; PVK/WO₃ heterojunction; Low temperature

1. Introduction

Ultraviolet (UV) radiation is part of solar radiation and is harmful to human health if overexposed. Therefore, there is a demand for UV monitoring and the key component of such technology is a large-area, high performance UV photodetector, which is a sensor that converts electromagnetic radiation signal into electronic signal based on the photoelectric effect principle. UV photodetectors are also widely used in other fields, such as space communications, material characterizations, and flame and ozone detection, etc. [1-3]. To date, many different wide bandgap metal oxide semiconductors, such as ZnO, Ga_2O_3, NiO, TiO_2, SnO_2 and WO_3, have been studied to produce UV photodetectors having different device structures [4-11]. However, metal-semiconductor-metal (MSM) ohmic contact photodetectors must rely on an external power source to operate. Considering the increasing energy demand, the development of high performance self-powered UV photodetectors, such as Schottky junction and heterojunction photodetectors, are highly desirable [12]. Furthermore, these self-powered photodetectors can find many new and exciting applications. The mechanism of self-powered photodetection can be summarized as three processes, for example, the generation of electron-hole pairs by the optical absorption of photosensitive materials, the separation of photogenerated electron-hole pairs by the built-in electric field and the collection of photogenerated carriers by the electrodes [13].

WO_3, a n-type semiconductor with direct bandgap, has recently attracted much attention for its potential application in photodetection due to its excellent optical, electronic and non-stoichiometric (the presence of a large number of oxygen vacancies in the lattice) properties [14]. So far, the research activities on tungsten oxide-based heterostructures are mainly focused on n-n heterojunction (e.g., β-Ga_2O_3/WO_3 [12], WO_3/In_2O_3 [15], WO_{3-x}/Si [16], WS_2/WO_3 [17]) and p-n heterojunction (e.g., WO_3/diamond [18], SWCNT/WO_3 [19], Al:WO_3/Si [20]). Among them, the UV photodetector based on β-Ga_2O_3/WO_3 nanoparticles has demonstrated self-powered characteristic. In addition, the above-mentioned inorganic device would require the use of expensive equipment for device fabrication at high vacuum and high temperature (400-1400 °C), which limits the production of large-area photodetectors [21]. The development of tungsten oxide-based self-powered photodetector still remains a challenge. However, organic device offers many advantages, such as low-cost, facile preparation at low temperature, and large-area device can be fabricated [22, 23]. Hence, it is of great interest to study photodetector that is based on organic-inorganic heterojunction as it is suitable for mass-production of large-area device at relatively low cost and it could form the built-in electric field to separate photogenerated carriers. Many organic-inorganic hybrid photodetectors have been reported, for example, poly(9-vinylcarbazole) (PVK)/ZnO nanorods/Gr [24], ZnO/PVK/Cu_2O nanorods [25], poly(3,4-ethylene-dioxythiophene):poly(styrenesulfonate) (PEDOT:PSS)/ZnO nanorod array [26], polyaniline (PANI)/ZnO core-shell microwire [27], PEDOT:PSS/Ga_2O_3 [13], β-Ga_2O_3/PANI [28] and NiO/PVK/ZnO [29]. Among them, PVK is the preferred organic polymer for UV photodetector due to its commercial availability, compatibility as a hole layer with multiple auxiliary material types, and direct and wide bandgap (~3.6 eV) [30]. PEDOT:PSS is another polymer with

adjustable conductivity and high mobility (~1.7 $cm^2V^{-1}S^{-1}$) [31]. Therefore, PEDOT:PSS is often used as a hole transport layer in the design and integration of organic optoelectronic devices. To the best of our knowledge, a photodetector with the structure of PEDOT:PSS/PVK/WO_3 has not been reported.

In this paper, a novel UV photodetector based on PVK/amorphous-WO_3 organic-inorganic heterojunction with PEDOT:PSS as a hole transport layer was produced and studied. The device was fabricated using a two-step preparation method, which comprised of spin-coating and sputtering. The WO_3-based heterostructure was prepared at low temperature (≤120 °C) and is compatible with the well-established CMOS technology, hence it can potentially be used in flexible electronics and imaging devices. The effect of WO_3, PVK and PEDOT:PSS layers at different preparation parameters on the performances of photodetector is discussed. An optimized PEDOT:PSS/PVK/WO_3 photodetector under certain parameters exhibited typical rectification characteristic and high photo-dark current ratio. More importantly, the device can operate at zero bias, therefore implying that it is possible to operate without external power source. It also demonstrated high responsivity (~10^1 AW^{-1}) and detectivity (~10^{13} Jones) under 365 nm irradiation at reverse bias.

2. Experimental

2.1 Materials

Tungsten target (W, 99.999%) was purchased from Zhongnuo Advanced Material (Beijing) Technology Co. Ltd. PVK and PEDOT:PSS (1.3 - 1.7 wt% dispersion in H_2O) were purchased from Xi'an Polymer Light Technology Corp. ITO-coated glass substrate (7 - 10 Ω/sq) was purchased from Microcrystalline Semiconductor Materials (Suzhou) Co. Ltd. All chemical reagents were used without further purification.

2.2 Device fabrication

The substrates were cleaned in a mixed solution of ammonia water, hydrogen peroxide and deionized water at 80 °C for 30 min, and then blown dried with nitrogen prior to use. Ultrasound-treated PEDOT:PSS aqueous dispersion (200, 300 and 500 μL) was spin-coated onto the clean substrates at 3000 rpm and baked at 120 °C for 15 min. This was followed by dissolving PVK solution (5, 10 and 20 mg/mL) in chloroform and then spin-coating it onto the prepared PEDOT:PSS layer at 2500 rpm, and baked at 60 °C for 20 min. WO_3 film was then deposited onto the prepared PVK layer by magnetron sputtering at room temperature, chamber vacuum pressure of less than $6.9×10^{-4}$ Pa, sputtering power of 100 W, ratio of oxygen and argon at 1:3 and sputtering durations of 400, 1350 and 2400 s. Finally, Al electrodes were deposited by thermal evaporation on top of the prepared WO_3 layer, and the photoactive area (2×2 mm^2) of the photodetector was defined by a shadow mask. Several UV photodetectors (i.e., D1#-D7#) comprising of ITO/PEDOT:PSS/PVK/WO_3/Al with different fabrication parameters were produced. The corresponding parameters and device numbers are listed in Table 1.

Table 1. Parameters of the different layers and associated device number.

Structure	Sputtering duration of WO_3 (s)	Concentration of PVK (mg/mL)	Volume of PEDOT:PSS (μL)	Device number
	400	10	300	D1#
	2400	10	300	D2#
ITO/PEDOT:PSS/PVK/WO_3/Al	1350	5	300	D3#
	1350	20	300	D4#
	1350	10	200	D5#
	1350	10	500	D6#
	1350	10	300	D7#

2.3 Instruments and characterization

Absorption characteristics of the films (e.g., WO_3, PVK, PEDOT:PSS and ITO) were studied using UV-Vis spectroscopy (iHR-320). Structural characteristics of the films (e.g., WO_3, PVK and PEDOT:PSS) were investigated using Raman spectroscopy (inVia). The WO_3 films were studied using multi-techniques, such as ultraviolet photoelectron spectroscopy (UPS, ESCALAB Xi[+]) with He-I excitation source (21.22 eV), X-ray photoelectron spectroscopy (XPS, K-Alpha[+]) with a monochromatic Al Kα radiation source (1486.6 eV), X-ray diffraction (XRD, EMPYREAN), transmission electron microscope (TEM, JEM-2100) and atomic force microscope (AFM, SPA-400). Cross-sectional image of the PEDOT:PSS/PVK/WO_3 photodetector was acquired using scanning electron microscope (SEM, Hitachi S-3400N).

Current-voltage (*I-V*) and transient response (*I-t*) measurements on the photodetectors were performed by a Keithley 2400 source meter. The *I-t* measurements were carried out with LED driven by function/arbitrary waveform generator (RIGOL, DG 1022U). All measurements were conducted at room temperature.

3. Results and discussion

TEM image of WO_3 is shown in Fig. 1(a). An enlarged TEM image of the selected area in Fig. 1(a) is shown in Fig. 1(b). The inset of Fig. 1(b) shows the electron diffraction pattern. It is found that the WO_3 sputtered at room temperature was amorphous, which is consistent with the XRD results in Fig. S1. Fig. 1(c) shows the Raman spectrum of WO_3 on Si substrate, which has five peaks at 132, 186, 267, 706 and 805 cm^{-1}. The higher wavenumber peaks at 706 and 805 cm^{-1} are associated with O-W-O stretching vibration mode, while the lower wavenumber peaks at 267, 186 and 132 cm^{-1} are related to W-O-W bending vibration mode as well as lattice mode (i.e., 186 and 132 cm^{-1}) [19, 32]. Raman spectra of PEDOT:PSS and PVK on quartz substrate are shown in Fig. 1(d). The PEDOT polymer structure of the PEDOT:PSS are clearly visible in the Raman spectrum (between 1250 and 1600 cm^{-1}), however the PSS has

negligible contribution to the spectrum. The result is in good agreement with previously reported work [33]. As for the Raman spectrum of PVK, the following characteristic peaks are observed, for example, 1626 cm^{-1} corresponds to C-C stretching in the benzene ring, 1451 and 1492 cm^{-1} correspond to C-H deformation in benzene ring C=N^{+} stretching, 1235 cm^{-1} corresponds to the wagging of methylene in polyvinyl C-N stretching, and 1022 cm^{-1} corresponds to rocking-twisting of methylene in polyvinyl. These peaks are also consistent with previous work [23, 34]. Normalized UV-Vis absorption spectra of WO$_3$ and PVK are shown in Fig. 1(e) and (f), respectively. Both WO$_3$ and PVK films exhibited strong absorption in the UV band, thus implying they are suitable for detecting UV light. For WO$_3$, a steep absorption edge can be observed at ~330 nm. For PVK, five absorption bands are evident at ~232, 264, 295, 332 and 345 nm that correspond to the excitation of delocalized PVK electrons. The absorption is mainly attributed to π-π* and n-π* transition of the carbazole groups [35, 36]. The observed absorption characteristics of PVK are consistent with previously reported work [23]. In general, the optical bandgap (E_g) of organic polymers corresponds to the initial light absorption, that is, the absorption edge corresponding to the longest wavelength [29]. The insets of Fig. 1(e) and (f) are estimated plots of $[\alpha(h\nu)]^2$ versus photon energy ($h\nu$) for WO$_3$ and PVK, respectively. The E_g can be estimated by the following equation:

$$\alpha(h\nu) = A\sqrt{(h\nu - E_g)} \qquad (1)$$

where α is optical absorption coefficient associated with $h\nu$ and A is a constant. According to the film thickness estimated from the SEM image (see Fig. 4(a)), the E_g of WO$_3$ and PVK films can be calculated as 3.87 and 3.50 eV, respectively. The insets of Fig. 1(e) and (f) show the AFM 3D images (having a scale of 10 μm×10 μm) of the WO$_3$ and PVK films with measured root-mean-square surface roughness of 0.94 and 3.92 nm, respectively.

The energy band of the amorphous WO$_3$ was studied using UPS as shown in Fig. 1(g). The binding energy of the secondary cut-off ($E_{cut-off}$) was at 18.78 eV, and the difference between the valence band maximum (VBM) and the Fermi level (E_F) was 3.14 eV. Therefore, the work function (W) can be calculated using the equation below [37]:

$$W = h\nu - E_{cut-off} \qquad (2)$$

where $h\nu$ is photon energy (21.22 eV). Taking into consideration of the E_g of WO$_3$ (3.87 eV) obtained from the inset of Fig. 1(e), the calculated values of W, VBM and conduction band minimum (CBM) were 2.44, 5.56 and 1.69 eV, respectively. XPS studies were performed to investigate the chemical states and atomic ratio of W and O in the WO$_3$. Fig. 1(h) and (i) show XPS spectra on W4f and O1s core level peaks, respectively. The C element observed from the XPS survey spectrum (see Fig. S2) was adventitious carbon, and the ratio of W and O was ~3.12 through quantitative analysis, as shown in Table S1. The peaks at binding energy of 41.5, 37.9 and 35.7 eV (in Fig. 1(h)) correspond to W5p$_{3/2}$, W4f$_{5/2}$ and W4f$_{7/2}$, respectively. The results imply that the W in the film is in its highest oxidation state of W^{6+}. This is in good agreement with

previously reports on WO$_3$ [38, 39]. In addition, the O1s peaks in Fig. 1(i) were located at 532.0 and 530.5 eV after Gaussian fitting. The peak at low binding energy (i.e., 530.5 eV) is related to the lattice oxygen (O$_L$) in the WO$_3$, while the peak at high binding energy (i.e., 532.0 eV) is associated with absorbed oxygen (O$_A$) at the surface of the WO$_3$ grain [39, 40].
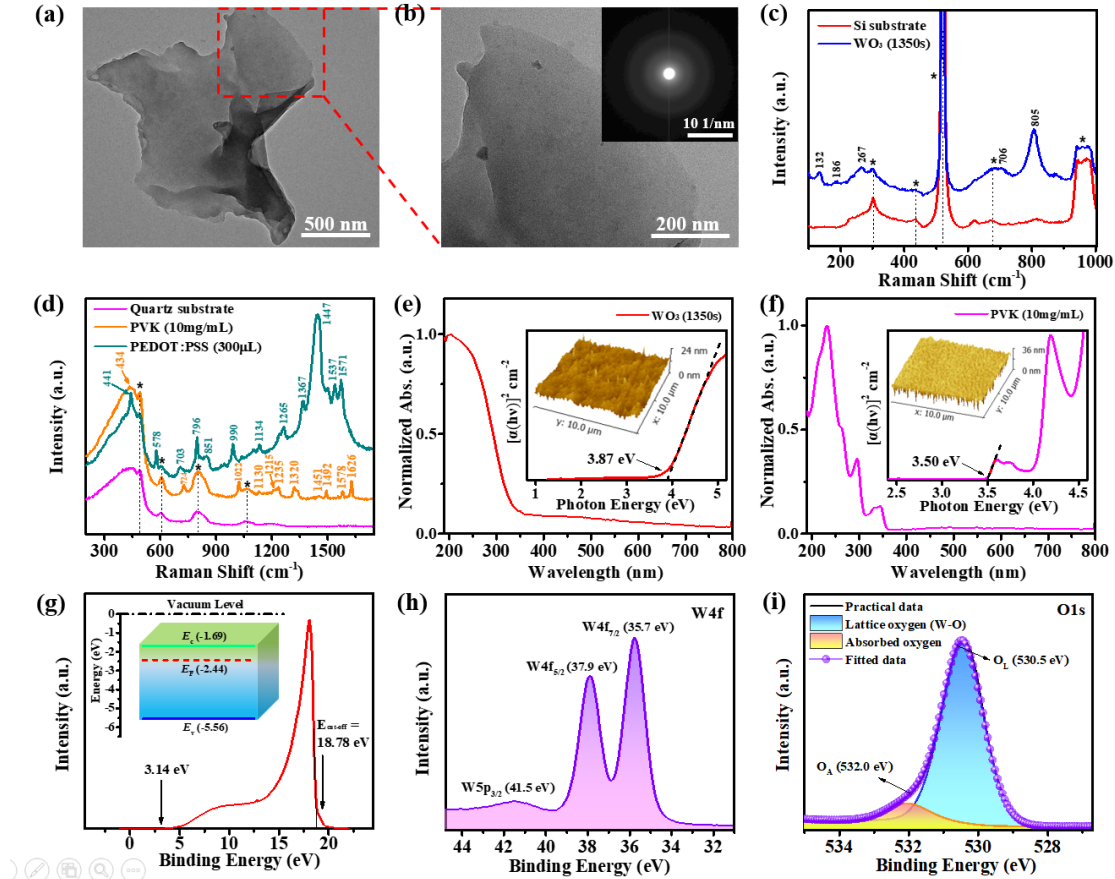

Fig. 1. (a) TEM image and (b) corresponding enlarged TEM image of WO$_3$ (Inset: Electron diffraction pattern). (c) Raman spectra of substrate and WO$_3$. (d) Raman spectra of substrate, PVK and PEDOT:PSS. (e) Normalized UV-Vis absorption spectrum of WO$_3$ (Inset: Plot of $[\alpha(h\nu)]^2$ versus photon energy and AFM 3D image of WO$_3$). (f) Normalized UV-Vis absorption spectrum of PVK (Inset: Plot of $[\alpha(h\nu)]^2$ versus photon energy and AFM 3D image of PVK). (g) UPS spectrum of WO$_3$ (Inset: Energy level diagram of WO$_3$). (h) and (i) XPS spectra of W4f and O1s core levels of WO$_3$, respectively.

Fig. 2(a) depicts the fabrication process of the PEDOT:PSS/PVK/WO$_3$ photodetectors. As shown, both PEDOT:PSS and PVK were spin-coated onto the cleaned ITO substrates and baked at low temperature after each coating process. This was followed by sputtering WO$_3$ film on top of the PVK layer at room temperature. Al electrodes were then vapor-deposited onto the as-prepared WO$_3$ film by using a shadow mask. Finally, gold wires were attached to the ITO and Al electrodes using silver paste as the bottom and top electrodes, respectively. It should be noted that a total of seven devices were fabricated using different preparation parameters of the layers (i.e., WO$_3$, PVK and PEDOT:PSS) as part of device optimization process. These devices have various combinations of preparation parameters, such as different sputtering durations

of WO$_3$ (400, 1350 and 2400 s), concentrations of PVK (5, 10 and 20 mg/mL) and volume of PEDOT:PSS (200, 300 and 500 µL). They were namely, D1# (PEDOT:PSS-300/PVK-10/WO$_3$-400), D2# (PEDOT:PSS-300/PVK-10/WO$_3$-2400), D3# (PEDOT:PSS-300/PVK-5/WO$_3$-1350), D4# (PEDOT:PSS-300/PVK-20/WO$_3$-1350), D5# (PEDOT:PSS-200/PVK-10/WO$_3$-1350), D6# (PEDOT:PSS-500/PVK-10/WO$_3$-1350) and D7# (PEDOT:PSS-300/PVK-10/WO$_3$-1350). For the purpose of device comparison, other preparation and characterization conditions of the devices D1# to D7# were kept the same. In order to evaluate the photoelectric characteristics of these devices, the transient response to an incident light at 0 V bias with a frequency of 0.1 Hz and an intensity of 1.57 mWcm^{-2} (365 nm UV light) by turning on and off the light source was measured on the devices as shown in Fig. 2(b). The current of all the devices (i.e., D1#-D7#) increased or decreased immediately to different extents when the light was turned on or off, respectively. It can be seen that the photodetectors consisting of PEDOT:PSS/PVK/WO$_3$ exhibited good reproducibility and self-powered characteristics. This means that the device does not need external power source for its operation and is ideal for remote operation when electricity is not readily available. Compared with the device D1#, D2#, D3#, D4# and D5#, the device D6# and D7# revealed much lower dark current and much higher photoresponse. The photocurrent peak of D6# and D7# was ~3.7 and 4.1 nA, respectively, and their on/off ratio was significantly larger. The dark current of D7# was ~0.061 nA with a maximum on/off ratio of ~67 at 0 V. This demonstrates that the different sputtering durations of WO$_3$, concentrations of PVK and volumes of PEDOT:PSS could affect the photoelectric properties of the devices to varying degrees. Therefore, the results in Fig. 2(b) were normalized (as shown in Fig. 3(d), (e) and (f)) in order to compare their photoresponse.
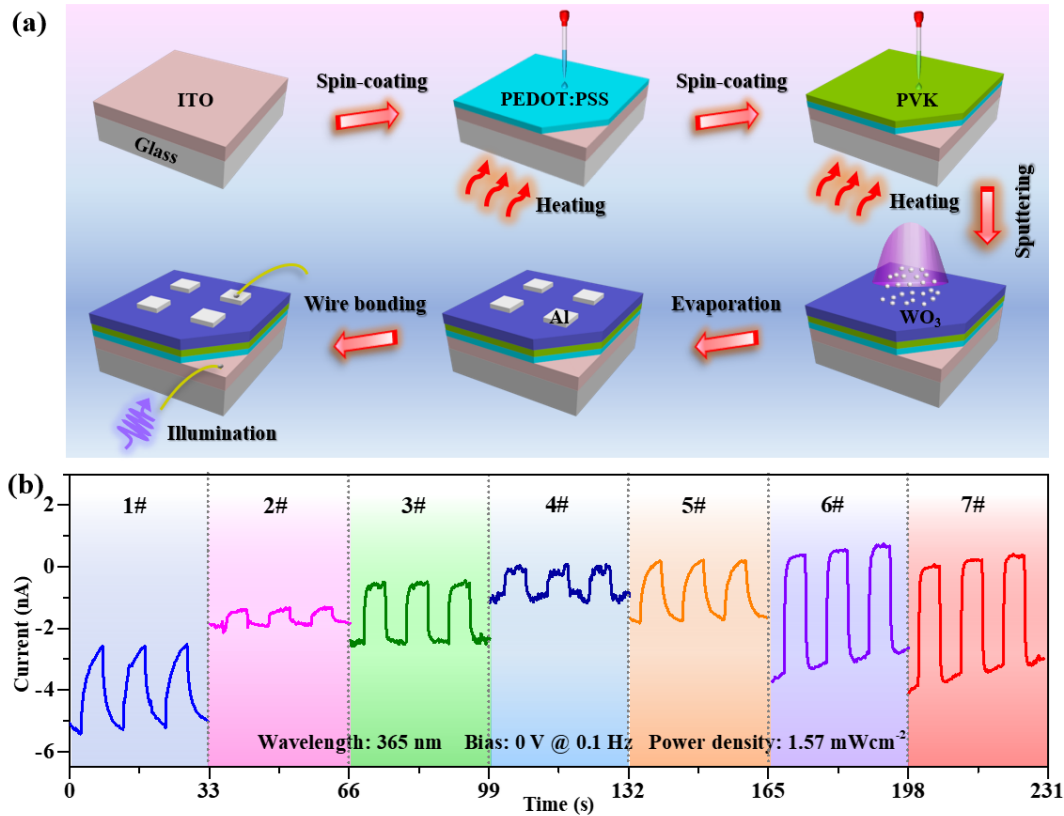
Fig. 2. (a) Schematic diagrams illustrating the fabrication process of the PEDOT:PSS/PVK/WO$_3$ photodetector. (b) Transient response of the PEDOT:PSS/PVK/WO$_3$ photodetectors (i.e., D1#-D7#) at 0 V under 365 nm illumination with optical power density of 1.57 mWcm^{-2}.

The effect of the different layers (i.e., WO$_3$, PVK and PEDOT:PSS) on the photoelectric properties of PEDOT:PSS/PVK/WO$_3$ photodetectors was investigated. Fig. 3(a), (b) and (c) show enlarged log *I-V* characteristics of the devices D1#-D7# from -2 V to -1 V under dark and 365 nm light with an intensity of 5.19 mWcm^{-2}. Fig. S3 shows the log *I-V* characteristics of the devices from -2 V to 2 V. The dark current and photocurrent of all devices increased slightly with an increase in the applied bias. The effect of different sputtering durations (i.e., 400, 1350 and 2400 s) of WO$_3$ on the devices, such as D1# (400 s), D7# (1350 s) and D2# (2400 s), can be determined from Fig. 3(a). At -2 V bias, the dark current of D7# is slightly higher than that of D1# and D2#. But, D7# has much larger photocurrent of 2.49 mA at -2 V, which is nearly two orders of magnitude more than that of D1# (0.094 mA) and D2# (0.012 mA). Therefore, the photo-dark current ratio (I$_{photo}$/I$_{dark}$) at -2 V/-1 V of D1#, D2# and D7# were 57/37, 3/9 and 162/3071, respectively. It can be concluded that the device (i.e., D7#) with WO$_3$ sputtering duration of 1350s has a favorable *I-V* characteristic. Next, the effect of different concentrations of PVK (5, 10 and 20 mg/mL) on the devices, namely D3# (5 mg/mL), D7# (10 mg/mL) and D4# (20 mg/mL), can be investigated from Fig. 3(b). The dark current of D4# was much smaller than D3# and D7#, and its photocurrent was also significantly smaller. This is due to the excessively large PVK concentration, which can be seen as a parallel resistance to the device, resulting in poor photoresponse. The I$_{photo}$/I$_{dark}$ at -2 V/-1 V of D3# and D4# were 6/14 and 13/140, respectively. It

8

reached the maximum values for both -2 V and -1 V when the concentration of PVK was 10 mg/mL (i.e., D7#). Finally, the effect of different volumes of PEDOT:PSS (200, 300 and 500 µL) on the devices, namely D5# (200 µL), D7# (300 µL) and D6# (500 µL), can be studied from Fig. 3(c). The dark current of D5# (~1.49 µA) was slightly smaller than that of D7# and D6# at -2 V but they were of similar magnitude at -1 V (within a few tenths of a µA). However, the photocurrent (8.07/1.84 µA at -2/-1 V) of D5# was two orders of magnitude smaller than that of D7# and D6# (having mA magnitude). The I_{photo}/I_{dark} reached the maximum when the volume of PEDOT:PSS was 300 µL (i.e., D7#). Among all devices, the I_{photo}/I_{dark} of D6# was second only to D7#, as summarized in Fig. 3(g). The plots of photocurrent and I_{photo}/I_{dark} of the devices (i.e., D1#-D7#) with different preparation conditions were shown in Fig. S4(a) and (b). The photocurrent and I_{photo}/I_{dark} of the devices increased with an initial increase in sputtering duration of WO_3, concentration of PVK and volume of PEDOT:PSS. However, further increase in the sputtering duration, concentration and volume would lead to a reduction in both the photocurrent and I_{photo}/I_{dark} of the devices. Device D7# has an optimal photocurrent and I_{photo}/I_{dark} of 2.49 mA and 162, respectively, when the sputtering duration of WO_3 was 1350 s, concentration of PVK was 10 mg/mL, and volume of PEDOT:PSS was 300 µL. The thickness of the WO_3 and PVK photoactive layers, which can be affected by sputtering duration and concentration, is crucial to the performance of the device. For example, D1# and D3#, having relatively thin WO_3 (sputtering duration of 400 s, ~15 nm thick, see Fig. S5(a)) and PVK (concentration of 5 mg/mL, ~ 40 nm thick, see Fig. S5(d)) films, exhibited low light absorption and small photogenerated carriers resulting in a low photocurrent. In contrast, D2# and D4#, having relatively thick WO_3 (sputtering duration of 2400 s, ~88 nm thick, see Fig. S5(c)) and PVK (concentration of 20 mg/mL, ~196 nm thick, see Fig. S5(f)), could absorb more photons but the photo lifetime is limited. This would reduce the efficiency in carrier collection resulting in a low photoresponse.

To investigate the effect of the different layers (i.e., WO_3, PVK and PEDOT:PSS) on response time of the photodetectors (D1#-D7#), the measured *I-t* curves were normalized and fitted exponentially, as shown in Fig. 3(d), (e) and (f). The measurement conditions were the same as in Fig. 2(b). The rise time (τ_r) and decay time (τ_d) can be fitted by a biexponential relaxation equation below [41]:

$$I = I_0 + A\exp(-t/\tau_1) + B\exp(-t/\tau_2) \qquad (3)$$

where I_0 is steady state photocurrent, *t* is time, A and B are constants, and τ_1 and τ_2 are relaxation time constants. As shown in Fig. 3(d), the calculated τ_r and τ_d (e.g., τ_r/τ_d) of D1#, D2# and D7# were 1.48/3.02 s, 1.69/2.88 s and 0.12/0.15 s, respectively. Also, the τ_r and τ_d of D3#, D4# (see Fig. 3(e)), D5# and D6# (see Fig. 3(f)) were 0.16/0.39 s, 0.18/0.42 s, 1.37/1.88 s and 0.24/0.25 s, respectively. It is evident that D7# demonstrates the shortest response times as summarized in Fig. 3(h). Intuitively, the plots of response time of the devices (i.e., D1#-D7#) with different preparation conditions were shown in Fig. S4(c). With an increase in sputtering duration of WO_3, concentration of PVK and volume of PEDOT:PSS, both rise and decay time decreased initially and then increased with further increase in the sputtering duration,

concentration and volume. Again, D7# has an optimal rise and decay time of 0.12 and 0.15 s, respectively. Therefore, D7# represented the optimized PEDOT:PSS/PVK/WO$_3$ photodetector as it has the best photoelectric characteristics among all the seven devices when its sputtering duration of WO$_3$ was 1350s, the concentration of PVK was 10 mg/mL and the volume of PEDOT:PSS was 300 μL.
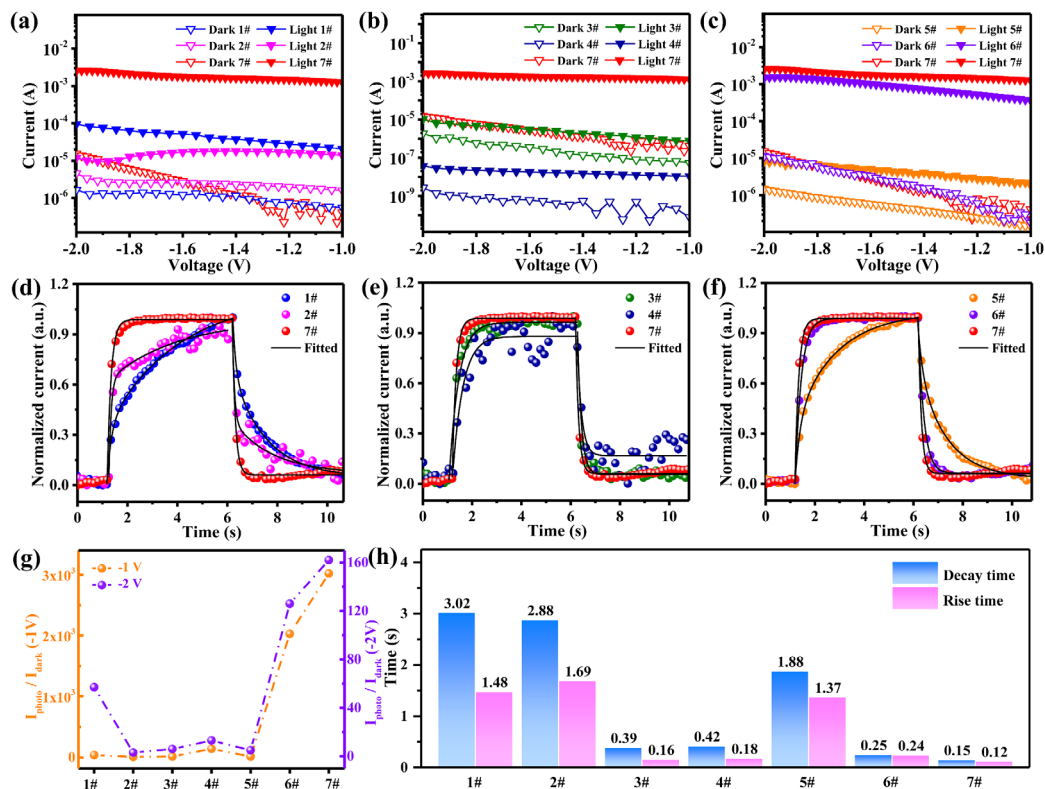

Fig. 3. Enlarged log *I-V* characteristics from -2 V to -1 V of photodetectors (a) D1#, D2# and D7#, (b) D3#, D4# and D7# and (c) D5#, D6# and D7# under dark and 365 nm light with optical power density of 5.19 mWcm^{-2}. (d)-(f) Normalized enlarged view of the rise/decay edges (from Fig. 2(b)) with fitted curves for the different photodetectors. (g) I$_{photo}$/I$_{dark}$ of the photodetectors (i.e., D1#-D7#) at -1 and -2 V. (h) Fitted rise/decay times of the photodetectors (i.e., D1#-D7#).

Further characterisations were carried out on device D7# to evaluate its performances and the following analysis is specifically for D7#. Fig. 4(a), (b) and (c) show the FESEM images of PVK, WO$_3$ and WO$_3$ deposited on PVK (i.e., PVK/WO$_3$), respectively. For PVK film, the FESEM image reveals a smooth morphology and absence of particles or aggregates, as shown in Fig. 4(a). Fig. 4(b) shows the surface of WO$_3$ film and reveals fine particles that are uniform and dense. Fig. 4(c) shows the morphology of WO$_3$ deposited on PVK. It can be seen that PVK/WO$_3$ film exhibits relatively uniform and dense granular surface due to the combination of smooth and grain films [42]. Fig. 4(d) shows the cross-sectional SEM image of the photodetector. The thickness of WO$_3$, PVK and PEDOT:PSS was measured to be ~49, 84 and 33 nm, respectively. The ohmic contact behavior between the Al electrode and WO$_3$ film was demonstrated, as shown in Fig. 4(e). It is worth noting that the WO$_3$ film (e.g., Al/WO$_3$/Al) is responsive to UV light. Fig. 4(f) shows log *I-V* characteristics of the photodetector under dark and light conditions. As shown in Fig. S6, light wavelength

greater than 350 nm can penetrate the ITO electrode and PEDOT:PSS hole transport layer, hence measurements on the device were performed by illuminating 365 nm UV light on the ITO side with optical power densities of 1.56 and 5.19 mWcm^{-2}. The *I-V* characteristic of the device under dark condition is shown in the inset of Fig. 4(e). There is a sharp increase in the dark current under positive bias (>1.4 V), which demonstrates a typical rectification behavior and the formation of the PVK/WO$_3$ heterostructure. When the photodetector was exposed to UV radiation, the reverse current increased sharply as shown in Fig. 4(f). Also, the current at 0 V increased from 0.52 μA to 8.83 μA, hence implying that the device can operate in a self-powered mode. Furthermore, an increase in the optical power density has resulted in an increase in the current. Therefore, the PEDOT:PSS/PVK/WO$_3$ photodetector can generate photogenerated carriers under UV light and be efficiently collected by the electrodes. Fig. 4(g) shows the transient response of the photodetector at 0 V under 365 nm light.

Figures of merit, such as responsivity (*R*), external quantum efficiency (EQE) and detectivity (*D**), are often used to evaluate the performance of photodetectors. The plots of *R* and EQE against bias voltage of the device are shown in Fig. 4(h). *R* and EQE can be calculated using the following equations [43, 44]:

$$R = J_{ph} / P_{opt} \qquad (4)$$

$$EQE = hcR_\lambda / (e\lambda) \qquad (5)$$

where J_{ph} is photocurrent density, P_{opt} is incident optical power, h is Planck constant, c is light speed, e is electron charge and λ is wavelength of incident light. Under negative bias, both *R* and EQE generally increased with increasing negative voltage, and exhibited larger values at higher optical power densities. The maximum values of *R* and EQE were 12.41 AW^{-1} and 4221 %, respectively, at bias voltage of -1.96 V and optical power density of 5.19 mWcm^{-2}. *R* and EQE of the photodetector at 0 V were 0.07 AW^{-1} and 23.68 %, respectively. When the optical power density increases to a suitable value, the photoactive layer can absorb light efficiently and produce photogenerated carriers, some of which are trapped by holes resulting in a large increase in electron concentration and a multiplication effect. This demonstrates high gain of the device and may attribute to the existence of oxygen-related hole-trap states at the surface of amorphous WO$_3$, hence leading to an increase in free electron concentration [44, 45]. Moreover, the high electron mobility (~12 cm^{2}V^{-1}s^{-1}) of WO$_3$ [46], the choice of hole transport layer (i.e., PEDOT:PSS) and the vertical device structure, which contribute to the shortening of the carrier transit time and therefore effectively reducing the recombination rate. The EQE of the other devices, such as D1#, D2#, D3#, D4#, D5# and D6#, were also calculated using the same method and were 276, 274, 646, 2.53, 208 and 2518 %, respectively. Detectivity (*D**) of the device can be determined using the equation [47, 48]:

$$D^* = R / \sqrt{2e|J_d|} \qquad (6)$$

where J_d is dark current density. By calculation, the maximum of *D** was 1.80×10^{13} Jones (cmHz$^{1/2}$W^{-1}) under 365 nm illumination at optical power density of 5.19 mWcm^{-2} and negative

bias of -0.6 V as shown in Fig. 4(i), and the average remained at 10^{12}. The D^* of the photodetector at 0 V was 3.4×10^{10} Jones. Thus, the PEDOT:PSS/PVK/WO$_3$ photodetector exhibited excellent R and D^*. R (see Fig. S7) and D^* (see Fig. S8) of the other devices (i.e., D1#, D2#, D3#, D4#, D5# and D6#) were also determined using the above equations. The performances of these seven devices were compared and summarized in Table 2. The plots of R, D^* and EQE for the devices with different preparation conditions are shown in Fig. S9 for comparison. Device D7# exhibited an optimal R, D^* and EQE of 12.41 AW^{-1}, 1.80×10^{13} Jones and 4221 %, respectively. In addition, Table S2 compares the device performance of this work with tungsten oxide-based [16, 49, 50] and other typical oxide-based [24-26, 51, 52] UV photodetectors. The comparison of R and D^* for the PEDOT:PSS/PVK/WO$_3$ photodetector with other UV photodetectors are depicted in Fig. 5(a). Table S3 compares the device performance of this work with other self-powered UV photodetectors [12, 13, 27, 53-60] consisting of oxide based heterostructures at 0 V. It can be seen that the self-powered UV photodetector (i.e., D7#) based on PVK/WO$_3$ heterojunction in this work demonstrates relatively high performances.
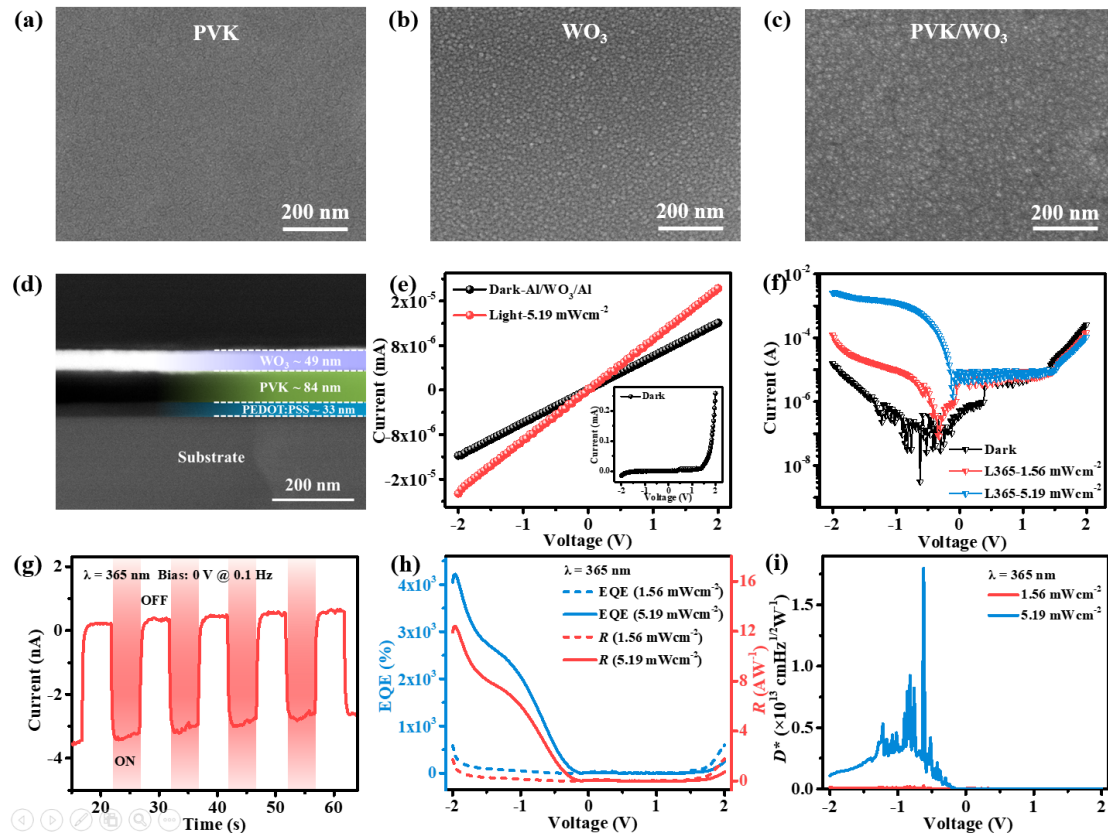

Fig. 4. FESEM images of (a) PVK, (b) WO$_3$ and (c) WO$_3$ deposited on PVK (i.e., PVK/WO$_3$). (d) Cross-sectional SEM image of the optimized PEDOT:PSS/PVK/WO$_3$ photodetector (i.e., D7#). (e) *I-V* plot of Al/WO$_3$/Al structure under dark and light conditions (Inset: *I-V* curve of the photodetector (i.e., D7#) under dark condition). (f) Log *I-V* curves of the photodetector (i.e., D7#) under dark and 365 nm light at different optical power densities (1.56 and 5.19 mWcm^{-2}). (g) Transient response of the photodetector (i.e., D7#) at 0 V under 365 nm light. (h) Plots of R and EQE against bias voltage of the photodetector (i.e., D7#) under 365 nm light. (i) Plots of D^* against bias voltage of the photodetector (i.e., D7#) under 365 nm light and at different optical power densities.

Understandably, the high performance of the photodetector is directly related to the photoelectric conversion mechanism of the PVK/WO$_3$ organic-inorganic heterojunction. The photoresponse of a semiconductor heterojunction, especially organic-inorganic heterojunction, is a complex process. To better understand the photoresponse mechanism at such heterojunction, the characteristics of semiconductor and organic polymer are considered in the discussion. The energy band diagram of any heterojunction depends on the electron affinity (χ), work function (W) and E_g of the two semiconductors that form the heterojunction. Herein, the HOMO and W of PVK are -5.8 and -5.55 eV, respectively, according to the reported literature [53]. Since the E_g of PVK is ~3.5 eV (from the UV-Vis absorption spectrum), the LUMO is therefore -2.3 eV. The χ, W and E_g of WO$_3$ are -1.69, -2.44 and 3.87 eV, respectively, as calculated from UPS and UV-Vis absorption spectra. The LUMO and HOMO of PEDOT:PSS are reported to be -3.3 and -5.3 eV, respectively [13]. Before contact, the energy level of each material is independent as shown in Fig. 5(b). When two semiconductor materials with opposite conductive types are contacted to form a heterojunction, electrons will flow from the n-type semiconductor (i.e., WO$_3$) to the p-type semiconductor (i.e., PVK) due to the high Fermi level position of the n-type semiconductor, while the holes flow in the opposite direction until the Fermi level is lined up. Fig. 5(c) shows the energy band diagram of the PVK/WO$_3$ heterojunction under dark condition after contact. At this moment, PVK and WO$_3$ have a unified Fermi level. A space charge region (i.e., barrier region) is formed at the interface due to the diffusion of carriers. The positive (negative) space charge region is situated at WO$_3$ (PVK) near the junction. The positive and negative space charge region will result in a built-in electric field at the junction. Due to the electric field, the energy band of PVK would bend downward at the interface to form a 'notch', while the energy band of WO$_3$ would bend upward to form a 'spike'. It is worth noting that the barrier region and band bending mostly occur on the side of WO$_3$ due to the weak intermolecular force of PVK. Here, an ideal interface is assumed where the traps are ignored. The different Fermi levels between PVK and WO$_3$ results in a built-in electric potential (V_b) of 3.11 eV (theoretical value). The band offset at the conduction band (ΔE_c) and valence band (ΔE_v) are 0.61 and 0.24 eV, respectively. When the photodetector based on PVK/WO$_3$ heterojunction is exposed to UV illumination (hv), the PVK mainly absorbs the light and its valence electrons transit into the conduction band upon gaining energy to generate electron-hole pairs. The large V_b is sufficient to separate the photogenerated electron-hole pairs. Driven by the built-in electric field, the electrons (e^-) move towards WO$_3$, while the holes (h^+) move towards PVK and are collected by the respective electrodes. Therefore, this explains the origin of photocurrent at zero bias as depicted in Fig. 5(d). When a forward bias voltage is applied to the PVK/WO$_3$ heterojunction, an electric field is generated in the opposite direction of the built-in electric field at the barrier region, as shown in Fig. 5(e). This results in a reduction of V_b and change to the Fermi level ($E_{F(WO_3)} > E_{F(PVK)}$) causing an increase in the barrier (i.e., 'spike'). Only electrons whose energy exceed the barrier height can transfer to PVK, which leads to a process of electron accumulation. This explains the phenomenon of 'plateau' in the forward current (in Fig. 4(c)). Conversely, as shown in Fig. 5(f), the built-in electric field at the barrier region is enhanced when a

reverse bias is applied, which results in a lower barrier height and a larger reverse current (see *I-V* curves in Fig. 4(c)). This explains the transport mechanism of carriers inside the heterojunction.
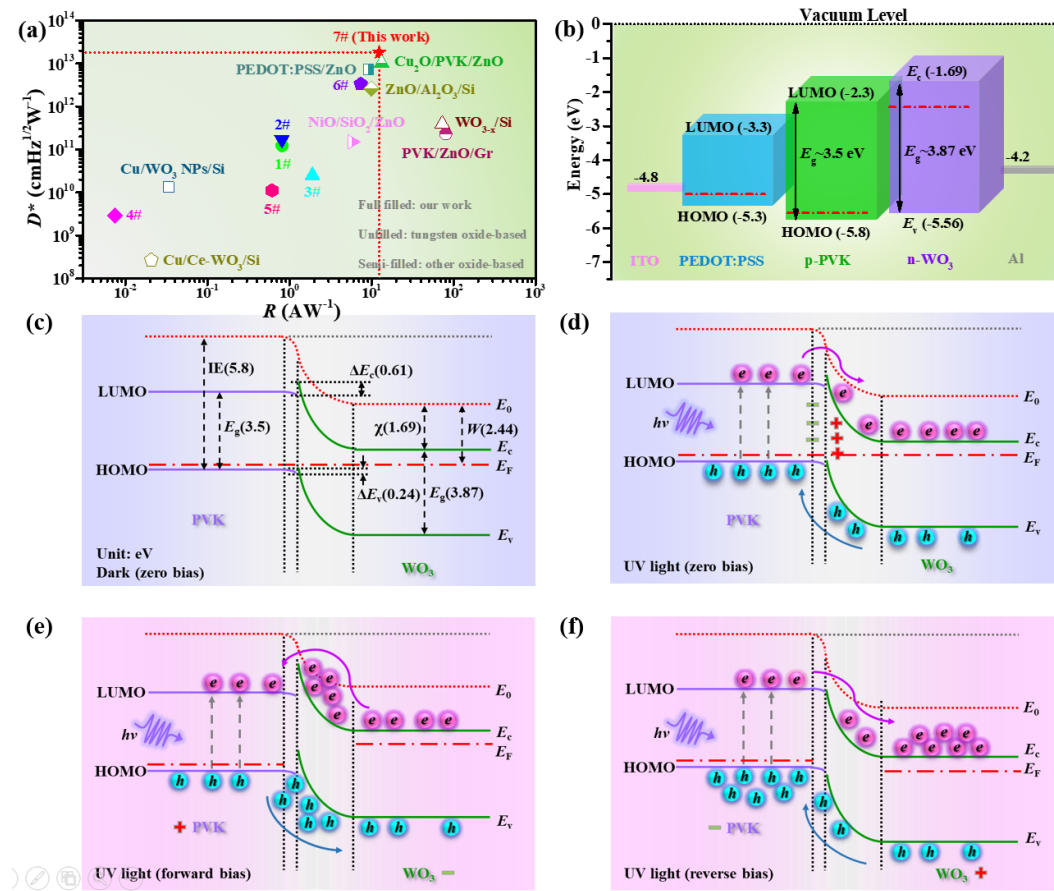

Fig. 5. (a) Comparison of maximum *R* and *D** for the PEDOT:PSS/PVK/WO₃ photodetectors (i.e., D1#-D7#) with other UV photodetectors (e.g., tungsten oxide-based and other common oxide-based photodetectors). (b) Schematic energy band diagram of the ITO/PEDOT:PSS/PVK/WO₃/Al photodetector before contact. (c) Energy band diagram of the PVK/WO₃ heterojunction after contact under dark condition. (d)-(f) Energy band diagrams of the PVK/WO₃ heterojunction under UV light at zero bias, forward bias and reverse bias, respectively.

14

Table 2. Comparison of performances of all seven devices in this work.

Structure	R (AW^{-1})	D^* (Jones)	EQE (%)	τ_r/τ_d (s)	I_{photo}/I_{dark} (-2 V)	Device
PEDOT:PSS-300/PVK-10/WO$_3$-	0.812	1.23×10^{11}	276	1.48/3.02	57	D1#
PEDOT:PSS-300/PVK-10/WO$_3$-	0.807	1.70×10^{11}	274	1.69/2.88	3	D2#
PEDOT:PSS-300/PVK-5/WO$_3$-	1.90	2.52×10^{10}	646	0.16/0.39	6	D3#
PEDOT:PSS-300/PVK-20/WO$_3$-	0.0075	2.89×10^{9}	2.53	0.18/0.42	13	D4#
PEDOT:PSS-200/PVK-10/WO$_3$-	0.61	1.12×10^{10}	208	1.37/1.88	5	D5#
PEDOT:PSS-500/PVK-10/WO$_3$-	7.40	3.32×10^{12}	2518	0.24/0.25	126	D6#
PEDOT:PSS-300/PVK-10/WO$_3$-	12.41	1.80×10^{13}	4221	0.12/0.15	162	D7#

4. Conclusion

In this work, self-powered UV photodetectors with the structure of PEDOT:PSS/PVK/WO$_3$ were successfully fabricated using a two-step method of spin-coating and sputtering at low temperature ($\leq$120 °C). PEDOT:PSS film was used as a hole transport layer. The observed rectification behavior was derived from the PVK/WO$_3$ organic-inorganic heterostructure. The preparation process of the photodetector was optimized and the PEDOT:PSS-300/PVK-10/WO$_3$-1350 photodetector exhibited the best photoelectric characteristics when the sputtering duration of WO$_3$ was 1350s, the concentration of PVK was 10 mg/mL and the volume of PEDOT:PSS was 300 μL. The calculated τ_r and τ_d of the photodetector were 0.12 and 0.15 s, respectively, at zero bias under 365 nm UV light. Such behavior is mainly due to the efficient separation of the photogenerated electron-hole pairs driven by the built-in electric field and collection by the electrodes. The photodetector also exhibited excellent R and EQE of 12.41 AW^{-1} and 4221 %, respectively, at bias voltage of -1.96 V and 365 nm light with optical power density of 5.19 mWcm^{-2}. Under the same light condition, the maximum D^* was 1.80×10^{13} Jones at negative bias (about -0.6 V). Furthermore, R, EQE and D^* of the photodetector at 0 V were 0.07 AW^{-1}, 23.68 % and 3.4×10^{10}, respectively. The low processing temperature, facile preparation process and excellent performance of the PEDOT:PSS/PVK/WO$_3$ photodetector is highly desirable for large-area UV imaging application.

CRediT authorship contribution statement

Menghan Jia: Investigation, Data curation, Software, Formal analysis, Writing – original draft, Writing – review & editing. **Libin Tang:** Conceptualization, Funding acquisition, Supervision, Resources, Validation, Methodology, Writing – review & editing. **Kar Seng Teng:** Writing – review & editing. **Yanfei Lü:** Conceptualization, Funding acquisition, Supervision, Validation, Writing – review & editing.

Declaration of Competing Interest

The authors declare that they have no known competing financial interests or personal relationships that could have appeared to influence the work reported in this paper.

Appendix A. Supplementary material

Supplementary data to this article can be found online at xxx.

References

[1] F. Teng, K. Hu, W. Ouyang, X. Fang, Photoelectric Detectors Based on Inorganic p-Type Semiconductor Materials, Adv Mater 30(35) (2018) e1706262.

[2] X. Wang, Q. Zhou, H. Li, C. Hu, L. Zhang, Y. Zhang, Y. Zhang, Y. Sui, B. Song, Self-powered ultraviolet vertical and lateral photovoltaic effect with fast-relaxation time in NdNiO3/Nb:SrTiO3 heterojunctions, Appl Phys Lett 112(12) (2018) 122103.

[3] P.V.K. Yadav, Y. Ashok Kumar Reddy, Controlled two-step synthesis of nanostructured WS2 thin films for enhanced UV–visible photodetector applications, Sensors and Actuators A: Physical 345 (2022) 113780.

[4] N. Nasiri, R. Bo, F. Wang, L. Fu, A. Tricoli, Ultraporous Electron-Depleted ZnO Nanoparticle Networks for Highly Sensitive Portable Visible-Blind UV Photodetectors, Adv Mater 27(29) (2015) 4336-4343.

[5] D. Guo, Q. Guo, Z. Chen, Z. Wu, P. Li, W. Tang, Review of Ga2O3-based optoelectronic devices, Materials Today Physics 11 (2019) 100157.

[6] S. Ghosh, M. Baral, R. Kamparath, S.D. Singh, T. Ganguli, Investigations on band commutativity at all oxide p-type NiO/n-type β-Ga2O3 heterojunction using photoelectron spectroscopy, Appl Phys Lett 115(25) (2019).

[7] G. Liu, M. Zhang, D. Zhang, X. Gu, F. Meng, S. Wen, Y. Chen, S. Ruan, Effects of growth substrates on the morphologies of TiO2 nanowire arrays and the performance of assembled UV detectors, Appl Surf Sci 315(oct.1) (2014) 55-58.

[8] H. Chen, L. Hu, X. Fang, L. Wu, General Fabrication of Monolayer SnO2 Nanonets for High-Performance Ultraviolet Photodetectors, Adv Funct Mater 22(6) (2012) 1229-1235.

[9] A. Moudgil, V. Dhyani, S. Das, High speed efficient ultraviolet photodetector based on 500 nm width multiple WO3 nanowires, Appl Phys Lett 113(10) (2018).

[10] P.V. Karthik Yadav, B. Ajitha, Y.A.K. Reddy, V.R. Minnam Reddy, M. Reddeppa, M.-D. Kim, Effect of sputter pressure on UV photodetector performance of WO3 thin films, Appl Surf Sci 536 (2021) 147947.

[11] P.V.K. Yadav, Y.A.K. Reddy, B. Ajitha, V.R. Minnam Reddy, Oxygen partial pressure dependent UV photodetector performance of WO3 sputtered thin films, J Alloy Compd 816 (2020) 152565.

[12] S. Li, J.-Y. Yue, C. Wu, Z. Liu, Z.-Y. Yan, P.-G. Li, D.-Y. Guo, Z.-P. Wu, Y.-F. Guo, W.-H. Tang, Self-Powered Ultraviolet Photodetector Based on β-Ga2O3/WO3 NPs Heterojunction With Low Noise and High Visible Rejection, IEEE Sensors Journal 21(23) (2021) 26724-26730.

[13] S. Li, Z. Yan, Z. Liu, J. Chen, Y. Zhi, D. Guo, P. Li, Z. Wu, W. Tang, A self-powered solar-blind photodetector with largeVocenhancing performance based on the PEDOT:PSS/Ga2O3organic–inorganic hybrid heterojunction, J Mater Chem C 8(4) (2020) 1292-1300.

[14] R.S. Vemuri, K.K. Bharathi, S.K. Gullapalli, C.V. Ramana, Effect of structure and size on the electrical properties of nanocrystalline WO3 films, Acs Appl Mater Inter 2(9) (2010) 2623.

[15] C. Ngangbam, R. Rajkumari, L. Thoibileima, M.W. Alam, N.K. Singh, High Responsivity of GLAD Synthesized Isotype WO3/In2O3 Nanocluster, Ieee Photonic Tech L 33(17) (2021) 943-946.

[16] X. Zhang, Y. Su, Z. Tang, D. Hu, Z. Wang, Y. Hou, X. Wang, WO3-x/Si n-n homotype heterojunction with high performance photodetection characteristics, Scripta Materialia 189 (2020) 89-94.

[17] P.V.K. Yadav, Y.A.K. Reddy, WS2/WO3 Heterostructure-Based Photodetectors on SiO2/Si for Future Optoelectronics, ACS Applied Electronic Materials 5(5) (2023) 2538-2547.

[18] L. Wang, S. Cheng, C. Wu, K. Pei, Y. Song, H. Li, Q. Wang, D. Sang, Fabrication and high temperature electronic behaviors of n-WO3 nanorods/p-diamond heterojunction, Appl Phys Lett 110(5) (2017) 052106.

[19] N.M. Vuong, H.N. Hieu, D. Kim, An edge-contacted pn-heterojunction of a p-SWCNT/n-WO3 thin film, J Mater Chem C 1(33) (2013) 5153.

[20] M. Raja, J. Chandrasekaran, M. Balaji, P. Kathirvel, Investigation of microstructural, optical and dc electrical properties of spin coated Al:WO3 thin films for n-Al:WO3/p-Si heterojunction diodes, Optik 145 (2017) 169-180.

[21] W.U. Huynh, J.J. Dittmer, A.P. Alivisatos, Hybrid nanorod-polymer solar cells, Science 295(5564) (2002) 2425-7.

[22] F. Li, C. Ma, H. Wang, W. Hu, W. Yu, A.D. Sheikh, T. Wu, Ambipolar solution-processed hybrid perovskite phototransistors, Nat Commun (2015).

[23] J. Dai, S. Li, Z. Liu, Z. Yan, W. Tang, Fabrication of the PVK/ε-Ga2O3 organic-inorganic heterojunction diode towards solar-blind sensing application, Journal of Physics D Applied Physics (2021).

[24] X. Zhang, J. Zhang, B. Leng, J. Li, Z. Ma, W. Yang, F. Liu, B. Liu, Enhanced Performances of PVK/ZnO Nanorods/Graphene Heterostructure UV Photodetector via Piezo-Phototronic Interface Engineering, Advanced Materials Interfaces 6(23) (2019) 1901365.

[25] D.-C. Perng, H.-P. Lin, M.-H. Hong, High-performance ultraviolet detection and visible-blind photodetector based on Cu2O/ZnO nanorods with poly-(N-vinylcarbazole) intermediate layer, Appl Phys Lett 107(24) (2015).

[26] C. Kumar, A. Palwe, S. Rani, S. Saxena, S. Shukla, Fully Solution-Processed ZnO Nanorod Array/PEDOT:PSS Heterojunction Photodetector for Ultraviolet Light, Ieee Electr Device L 43(2) (2022) 260-263.

[27] Y. Chen, L. Su, M. Jiang, X. Fang, Switch type PANI/ZnO core-shell microwire heterojunction for UV photodetection, Journal of Materials Science & Technology (10) (2022) 7.

[28] Y. Wang, L. Li, H. Wang, L. Su, H. Chen, W. Bian, J. Ma, B. Li, Z. Liu, A. Shen, An ultrahigh responsivity self-powered solar-blind photodetector based on a centimeter-sized beta-Ga(2)O(3)/polyaniline heterojunction, Nanoscale 12(3) (2020) 1406-1413.

[29] J.D. Hwang, C.W. Fan, High-performance organic/inorganic hybrid ultraviolet p-NiO/PVK/n-ZnO heterojunction photodiodes with a poly(N-vinylcarbazole) insertion layer, J Mater Chem C (2019).

[30] S. Wang, S. Yang, C. Yang, Z. Li, W. Ge, Poly(N -vinylcarbazole) (PVK) Photoconductivity Enhancement Induced by Doping with CdS Nanocrystals through Chemical Hybridization, The Journal of Physical Chemistry B 104(50) (2000).

[31] J.P. Thomas, M.A. Rahman, S. Srivastava, J.S. Kang, D. Mcgillivray, M. Abd-Ellah, N.F. Heinig, K.T. Leung, Highly Conducting Hybrid Silver-Nanowire-Embedded Poly(3,4-ethylenedioxythiophene):Poly(styrenesulfonate) for High-Efficiency Planar Silicon/Organic Heterojunction Solar Cells, ACS nano 12(9) (2018) 9495-9503.

[32] S.I. Kim, S.K. Hyeong, S.P. Dong, S.H. Hyun, K. Heo, Performance enhancement of amorphous WO3 assisted graphene-based electronic devices: Aspect of surface engineering, Appl Surf Sci (2021) 149763.

[33] A.A. Farah, S.A. Rutledge, A. Schaarschmidt, R. Lai, J.P. Freedman, A.S. Helmy, Conductivity enhancement of poly(3,4-ethylenedioxythiophene)-poly(styrenesulfonate) films post-spincasting, J. Appl. Phys. 112 (11) (2012) 113709.

[34] N. Pei, X.T. Zhang, Y.C. Li, Y.B. Huang, Y.J. Mo, A study of poly (N -vinylcarbazole) adsorbed on silver surface by SERS, Vibrational Spectroscopy 21(1) (1999) 39-43.

[35] d.B.E. Barbosa, M.A. De, d.F.J. Nei, R. Valaski, F.V.M.M. De, Improved properties of high molar mass poly(9-vinylcarbazole) and performance as a light emitter compared with the commercial PVK, Materials Science & Engineering, B. Solid-State Materials for Advanced Technology (2022).

[36] L. Li, T.Q. Hu, C.R. Yin, L.H. Xie, Y. Yang, C. Wang, J.Y. Lin, M.D. Yi, S.H. Ye, W. Huang, A photo-stable and electrochemically stable poly(dumbbell-shaped molecules) for blue electrophosphorescent host materials, Polymer Chemistry 6(6) (2015) 983-988.

[37] W. Han, K. Liu, J. Yang, X. Chen, Q. Ai, Y. Zhu, Z. Cheng, B. Li, L. Liu, D. Shen, High-performance self-powered amorphous-BaTiO3/p-Si heterojunction photodetector controlled by ferroelectric effect, Appl Surf Sci 615 (2023) 156371.

[38] Guofa, Cai, Peter, Darmawan, Mengqi, Cui, Jiangxin, Wang, Jingwei, Chen, Highly Stable Transparent Conductive Silver Grid/PEDOT:PSS Electrodes for Integrated Bifunctional Flexible Electrochromic Supercapacitors, Advanced Energy Materials (2016).

[39] J. Zhang, H. Lu, L. Chang, C. Chen, X. Xia, Porous NiO–WO3 heterojunction nanofibers fabricated by electrospinning with enhanced gas sensing properties, Rsc Advances 7 (2017).

[40] C. Dong, L. Xu, H. Guan, C. Gang, Y. Wang, Combustion synthesized hierarchically porous WO3 for selective acetone sensing, Materials Chemistry & Physics 184 (2016).

[41] D.Y. Guo, Z.P. Wu, Y.H. An, X.C. Guo, X.L. Chu, C.L. Sun, L.H. Li, P.G. Li, W.H. Tang, Oxygen vacancy tuned Ohmic-Schottky conversion for enhanced performance in β-Ga2O3 solar-blind ultraviolet photodetectors, Appl Phys Lett 105(2) (2014) 031912.

[42] Y.A.K. Reddy, B. Ajitha, A. Sreedhar, E. Varrla, Enhanced UV photodetector performance in bi-layer TiO2/WO3 sputtered films, Appl Surf Sci 494 (2019) 575-582.

[43] X. Liu, L. Gu, Q. Zhang, J. Wu, Y. Long, Z. Fan, All-printable band-edge modulated ZnO nanowire photodetectors with ultra-high detectivity, Nat Commun 5 (2014).

[44] X. Xu, J. Chen, S. Cai, Z. Long, Y. Zhang, L. Su, S. He, C. Tang, P. Liu, H. Peng, X. Fang, A Real-Time Wearable UV-Radiation Monitor based on a High-Performance p-CuZnS/n-TiO2 Photodetector, Adv Mater 30(43) (2018) e1803165.

[45] Z. He, Q. Liu, H. Hou, F. Gao, B. Tang, W. Yang, Tailored Electrospinning of WO3 Nanobelts as Efficient Ultraviolet Photodetectors with Photo-Dark Current Ratios up to 1000, Acs Appl Mater Inter (2015).

[46] Y. Yao, D. Sang, L. Zou, Q. Wang, C. Liu, A Review on the Properties and Applications of WO(3) Nanostructure-Based Optical and Electronic Devices, Nanomaterials (Basel) 11(8) (2021).

[47] I.B. Khadka, N.R. Alluri, M.M. Alsardia, N.P.M. Joseph Raj, A.P.S. Prasanna, B. Ul Haq, S.J. Kim, S.-H. Kim, Ultra-low-power photodetector based on a high-photoresponse, plasmonic-effect-induced gateless quasi-freestanding graphene device, Appl Surf Sci 610 (2023) 155275.

[48] P.V.K. Yadav, B. Ajitha, Y.A. Kumar Reddy, V.R. Minnam Reddy, Enhanced Performance of WO3 Photodetectors Through Hybrid Graphene-Layer Integration, ACS Applied Electronic Materials 3(5) (2021) 2056-2066.

[49] R. Marnadu, J. Chandrasekaran, S. Maruthamuthu, V. Balasubramani, P. Vivek, R. Suresh, Ultra-high photoresponse with superiorly sensitive metal-insulator-semiconductor (MIS) structured diodes for UV photodetector application, Appl Surf Sci 480 (2019) 308-322.

[50] R. Marnadu, J. Chandrasekaran, S. Maruthamuthu, P. Vivek, V. Balasubramani, P. Balraju, Jet Nebulizer Sprayed WO3-Nanoplate Arrays for High-Photoresponsivity Based Metal–Insulator–Semiconductor Structured Schottky Barrier Diodes, J Inorg Organomet P 30(3) (2019) 731-748.

[51] Z. Huo, Y. Zhang, X. Han, W. Wu, W. Yang, X. Wang, M. Zhou, C. Pan, Piezo-phototronic effect enhanced performance of a p-ZnO NW based UV–Vis–NIR photodetector, Nano Energy 86 (2021) 106090.

[52] M. Jia, F. Wang, L. Tang, J. Xiang, K.S. Teng, S.P. Lau, Y. Lü, Low-power-consumption ultraviolet photodetector based on p-NiO/SiO2/n-ZnO, Optics & Laser Technology 157 (2023) 108634.

[53] Y. Dong, Y. Zou, J. Song, Z. Zhu, J. Li, H. Zeng, Self-Powered Fiber-shaped Wearable Omnidirectional Photodetectors, Nano Energy (2016) S2211285516304281.

[54] Y. Shen, X. Yan, H. Si, P. Lin, Y. Liu, Y. Sun, Y. Zhang, Improved Photoresponse Performance of Self-Powered ZnO/Spiro-MeOTAD Heterojunction Ultraviolet Photodetector by Piezo-Phototronic Effect, Acs Appl Mater Inter 8(9) (2016) 6137-6143.

[55] D.J. Lee, S.R. Ryu, G.M. Kumar, H.D. Cho, D.Y. Kim, P. Ilanchezhiyan, Piezo-phototronic effect triggered flexible UV photodetectors based on ZnO nanosheets/GaN nanorods arrays, Appl Surf Sci 558 (2021) 149896.

[56] B. Ouyang, K. Zhang, Y. Yang, Self-Powered UV Photodetector Array Based on P3HT/ZnO Nanowire Array Heterojunction, Advanced Materials Technologies (2017) 1700208.

[57] F. Cao, L. Jin, Y. Wu, X. Ji, High-performance, self-powered UV photodetector based on Au nanoparticles decorated ZnO/CuI heterostructure, J Alloy Compd 859 (2021) 158383.

[58] D. Guo, H. Liu, P. Li, Z. Wu, S. Wang, C. Cui, C. Li, W. Tang, Zero-Power-Consumption Solar-Blind Photodetector Based on beta-Ga2O3/NSTO Heterojunction, ACS Appl Mater Interfaces 9(2) (2017) 1619-1628.

[59] A self-powered deep-ultraviolet photodetector based on an epitaxial Ga2O3/Ga:ZnO heterojunction, J Mater Chem C 5 (2017).

[60] M. Wang, J. Zhang, Q. Xin, L. Yi, Z. Guo, Y. Wang, A. Song, Self-powered UV photodetectors and imaging arrays based on NiO/IGZO heterojunctions fabricated at room temperature, Opt Express 30(15) (2022) 27453-27461.